Research Article | Open Access

Microstructures

Zhu et al. Microstructures 2026, 6, 2026073 DOI:10.20517/microstructures.2025.160

High capacitive energy-storage in BNT-based Pb-free relaxors via dispersing strong long-range polarization within expanded lattice framework

Zhentao Zhu[1], Ji Zhang[2], Yifei Zha[1], Sixuan Wang[3], Zhihong Luo[4], Huajie Luo[1], Li-Feng Zhu[5], Laijun Liu[4], Guangzu Zhang[3], Hui Liu[1]

Keywords:
Capacitive energy-storage, $Bi_{0.5}Na_{0.5}TiO_3$, relaxors, local structure

Citation: Zhu, Z.; Zhang, J.; Zha, Y.; Wang, S.; Luo, Z.; Luo, H.; Zhu, L. F.; Liu, L.; Zhang, G.; Liu, H. High capacitive energy-storage in BNT-based Pb-free relaxors via dispersing strong long-range polarization within expanded lattice framework. *Microstructures* **2026**, *6*, 2026073. https://dx.doi.org/10.20517/microstructures.2025.160

Received: 29 Nov 2025 **First Decision:** 15 Jan 2026 **Revised:** 11 Mar 2026 **Accepted:** 12 Mar 2026 **Published:** 29 May 2026

Academic Editor: Jungho Ryu
Copy Editor: Xing-Yue Zhang
Production Editor: Xing-Yue Zhang

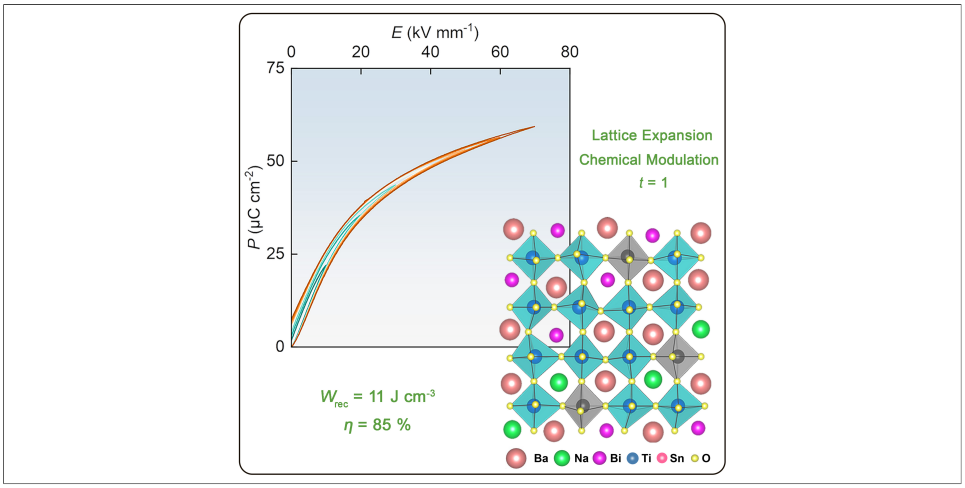

Abstract

The development of Pb-free dielectric materials with high recoverable energy-storage density (W_{rec}) and efficiency (η) remains a critical challenge for cutting-edge pulsed-power technologies. Herein, we propose a rational structural and chemical design to stabilize a relaxor state with tolerance factor t = 1.0096 by coupling highly distorted ferroelectric matrix with lattice-expanded component. We can disperse the strong long-range polarization within an expanded lattice framework through incorporating $BaSnO_3$ into $Bi_{0.5}Na_{0.5}TiO_3$-$BaTiO_3$ solid-solution with significant ferroelectric polarization, thereby achieving a synergistic optimization between the large intrinsic polarization and lattice structure. Neutron total scattering combined with Reverse Monte Carlo modeling, and atomic-resolution displacement mapping reveal Sn^{4+} disrupts strong long-range

[1]Beijing Advanced Innovation Center for Materials Genome Engineering, School of Advanced Materials Innovation, University of Science and Technology Beijing, Beijing 100083, China.
[2]School of Materials Science and Engineering, Nanjing University of Science and Technology, Nanjing 210094, Jiangsu, China.
[3]School of Integrated Circuits, Huazhong University of Science and Technology, Wuhan 430074, Hubei, China.
[4]College of Materials Science and Engineering, Guilin University of Technology, Guilin 541004, Guangxi AR, China.
[5]School of Materials Science and Engineering, University of Science and Technology Beijing, Beijing 100083, China.

Correspondence to: Dr. Ji Zhang, School of Materials Science and Engineering, Nanjing University of Science & Technology, Nanjing 210094, Jiangsu, China. E-mail: jizhang@njust.edu.cn; Dr. Huajie Luo, Prof. Hui Liu, Beijing Advanced Innovation Center for Materials Genome Engineering, School of Advanced Materials Innovation, University of Science and Technology Beijing, Beijing 100083, China. E-mail: hjluo@ustb.edu.cn; huiliu@ustb.edu.cn; Prof. Li-Feng Zhu, School of Materials Science and Engineering, University of Science and Technology Beijing, Beijing 100083, China. E-mail: zhu@ustb.edu.cn

polarization via *B*-site chemical frustration, generating polar nanoclusters with intense local distortions. Concurrently, Ba^{2+}-driven lattice expansion enhances polarization flexibility under electric fields. Notably, Bi^{3+}-enriched nanoregions retain unit-cell polarization up to 60 μC·cm^{-2}, confirming the coexistence of relaxor dynamics and strong local polar fluctuations. The optimized ceramic exhibits slim hysteresis loops with exceptional energy-storage performance (W_{rec} = 11 J·cm^{-3}, η = 85%), and excellent charge-discharge behavior (W_D = 7.0 J·cm^{-3} and P_D = 688 MW·cm^{-3}). This work establishes a paradigm for correlating microstructure and performance in Pb-free relaxors with high capacitive energy-storage.

INTRODUCTION

With the growing trend toward functional integration, compact design and extended longevity, pulsed-power devices are required to transit toward environmentally-friendly compositions, miniaturized and lightweight configurations, and high-performances. Dielectric capacitors, owing to their ultrafast charge-discharge rates, exceptional power density, and outstanding operational stability, have emerged as indispensable components in high-power pulsed systems, such as grid frequency regulation, industrial lasers, new energy vehicles, and advanced electromagnetic weaponry[1-6]. However, as energy-storage units increasingly pursue miniaturization and high integration, their relatively low energy density has become a critical bottleneck hindering broader applications[7,8]. For dielectric capacitors, ideal energy-storage ceramics must first exhibit both high recoverable energy-storage density (W_{rec}) and high energy-storage efficiency (η). These properties are governed by the polarization-electric field (*P*-*E*) hysteresis behavior, as defined by, $W_{rec} = \int_P^{P_m} E\mathrm{d}P$, $W_{tot} = \int_0^{P_m} E\mathrm{d}P$, $\eta = \frac{W_{rec}}{W}$ where P_m (maximum polarization), P_r (remanent polarization) and E determine energy storage performance[9-14]. Secondly, the pulse discharge performance in practical device applications is more directly reflected by the discharge energy density ($W_D = \frac{R\int I_{(t)}^2 \mathrm{d}t}{V}$, where R is resistance, I is current, t is time, and V is the volume of the dielectric capacitor), which characterizes the effective energy output of the system during dynamic processes[10]. Together, these two aspects determine the overall performance of devices under real operating conditions-high W_{rec} ensures energy storage capacity, while high W_D guarantees power delivery capability. Therefore, breaking the inherent compromise between W_{rec} and η while simultaneously enhancing the dynamic discharge characteristics related to W_D represents a key scientific challenge for achieving breakthroughs in next-generation high-performance pulsed-power devices[9,15-19].

Relaxor ferroelectrics (RFEs), with nanoscale polar heterogeneities that can rapidly respond to external electric fields, are widely considered as promising candidates to overcome above inverse relationship[10,13,20-22]. Recent advances, including via domain engineering[23,24], entropy tuning[2,13,25,26], and chemical framework design[17], have achieved significant breakthroughs in Pb-free RFEs[21,27,28]. Conventionally, RFEs are synthesized by incorporating various foreign ions into ferroelectric (FE) to disturb the long-range ferroelectric order[29-32]. However, the lack of systematic compositional design principles has led current research to rely largely on empirical trial-and-error approaches, rendering it challenging to simultaneously achieve an optimal trade-off between high W_{rec} and high η. This severely limits the rational design of high-performance dielectric capacitors for extreme-environment applications.

Herein, we propose a rational guidance for the Pb-free RFEs with outstanding capacitive energy-storage performance through local structure design and chemical modulation [Figure 1]. The enhancement of energy-storage density relies on a high P_m, which primarily originates from the moderate reorientation and extension of polarization vectors within the unit cell under an E[21]. Therefore, achieving high P_m hinges on constructing structural frameworks that host large intrinsic polarization vectors while providing sufficient spatial flexibility for polarization evolution. In perovskite structures, structural distortion (δ) is an indicator of the relative displacement of cations and anions within the lattice[33,34]. Among various Pb-free RFEs,

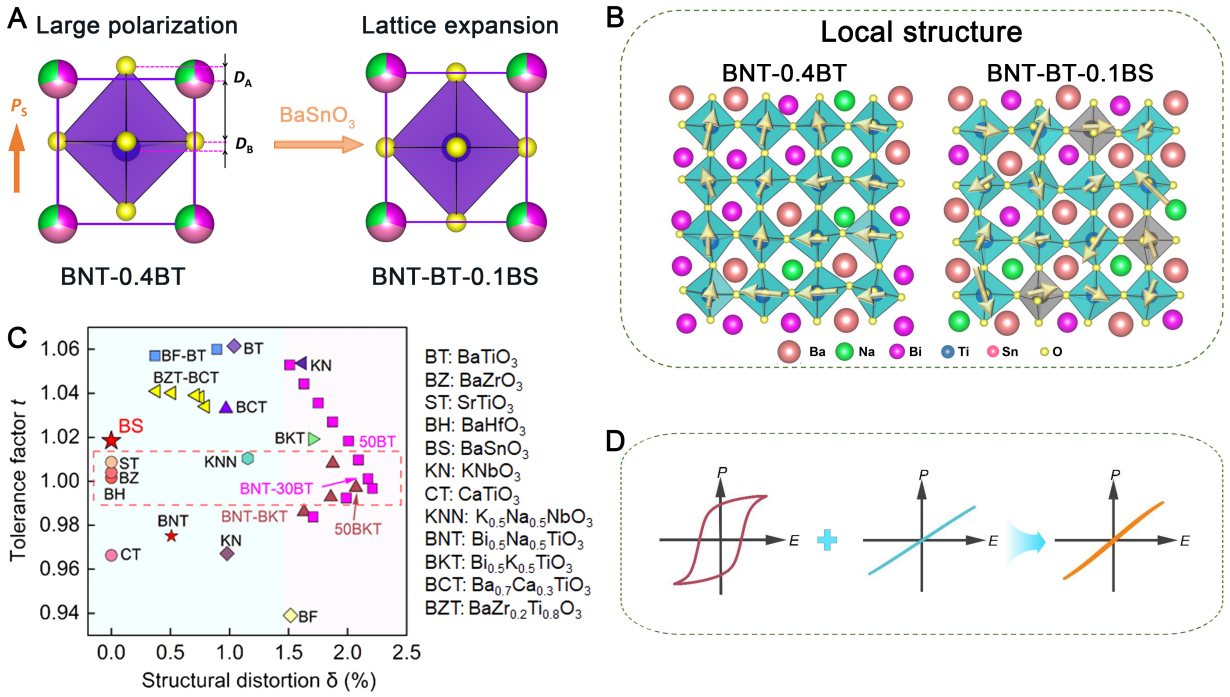

Figure 1. Local structure regulation and chemical design of energy-storage ceramics. (A) Structural evolution of BNT-BT perovskite after incorporating BS; (B) Schematic of the polar structure of BNT-0.4BT ferroelectric matrix and favorable BNT-BT-0.1BS RFEs; (C) Structural parameters of tolerance factor (t) and structural distortion (δ) for Pb-free perovskites; (D) Evolution of *P-E* loops. BNT: $Bi_{0.5}Na_{0.5}TiO_3$; BT: $BaTiO_3$; BS: $BaSnO_3$; RFEs: relaxor ferroelectrics.

$(1\text{-}x)Bi_{0.5}Na_{0.5}TiO_3\text{-}xBaTiO_3$ (BNT-xBT, $0.1 \le x \le 0.9$) systems exhibit relatively large δ [Figure 1C], enabling the inherent long-range ferroelectric orders and square polarization-electric field (*P-E*) loop with a large polarization and a high hysteresis loss [Figure 1D]. Furthermore, the structural distortion should occur within the perovskite framework, which is commonly judged by tolerance factor ($t = \frac{R_A+R_O}{\sqrt{2}(R_B+R_O)}$, where R_A, R_B and R_O are ionic radius for perovskites)[21]. The materials (such as $SrTiO_3$) with $t = 1$ generally indicate an ideal perovskite structure typically showing an ultrahigh η. As for $t > 1$ (such as $BaTiO_3$), the relatively smaller *B*-site ions have more space to deviate the center of BO_6, leading to a strong polarization [Figure 1C].

Based on above consideration, the paraelectric $BaSnO_3$ (BS) is introduced as an end-member into the ferroelectric BNT-0.4BT matrix with a high structural distortion. On the one hand, the large ionic radius of Ba^{2+} (1.61 Å) plays a critical role in promoting unit-cell expansion [Figure 1A], providing enhanced spatial flexibility for ion displacement under an external *E*, resulting in an amplified local polarization heterogeneity. Moreover, Sn^{4+} ions regulate the chemical environment of *B*-site cations and induce oxygen octahedral distortion, which disrupts atomic ordering and suppresses the coherence of long-range polarization. This process introduces random field effects while retaining strong local intrinsic polarization [Figure 1B]. On the other hand, combination of BNT-0.4BT with $t = 1.0076$ and BS with $t = 1.0184$ construct global perovskite structure with $t = 1.0096$, ensuring the stable RFE state with a high η [Figure 1C and D]. Accordingly, the RFE system not only preserves the intrinsic polarization strength of ferroelectrics but also generates a high density of locally symmetric polar clusters through atomic disordering.

MATERIALS AND METHODS

The $0.6Bi_{0.5}Na_{0.5}TiO_3\text{-}(0.4\text{-}x)BaTiO_3\text{-}xBaSnO_3$ ($x = 0$, 0.06, 0.10, 0.12) ceramics were synthesized via conventional solid-state reaction method. The raw material consisted of oxide and carbonate powders: Bi_2O_3(99.99%, Aladdin), Na_2CO_3(99.99%, Aladdin), TiO_2(99.9%, Aladdin), $BaCO_3$(99%, Macklin), and SnO_2

(99%, Macklin). The dried reactant powders were weighed according to the stoichiometric ratio and ball milled in anhydrous ethanol for 24 h. The mixture was subsequently dried at 100 °C for 120 min. The dried precursor powders were calcined in ambient atmosphere at 800-850 °C for 2 h. The calcined powders were mixed with polyvinyl alcohol (PVA) binder for granulation, and pressed into pellets with a diameter of 10 mm and a thickness of 1 mm. To reduce the volatilization of Bi and Na elements during sintering, the pellets covered with powder. After the removal of PVA at 550 °C for 2 h, the pellets were then sintered at 1,100 to 1,150 °C for 2 h. For electrical measurements at low electric fields, the sample thickness was 0.4-0.5 mm with an electrode area of approximately 56 mm^2. For energy-storage and charge-discharge measurements, the sample thickness was 50-60 μm and the electrode area was 0.8 mm^2.

The crystal structure was identified by the X-ray Diffractometer (Rigaku Smartlab3, Japan) with Cu Kalpha radiation at room temperature. Surface topography images of acid etched ceramic sample were captured by a field-emission scanning electron microscope (LEO1530, ZEISS SUPRA 55, Germany). Grain surface morphology, selected area electron diffraction (SAED), and high-resolution TEM images were acquired by an image aberration-corrected scanning transmission electron microscope (STEM, Titan ETEM G2, Thermo Fisher Scientific, USA) at the operating voltage of 300 kV. Atomic-scale high-angle annular dark-field (HAADF) phase images were acquired by a STEM (JEM-F200, JEOL, Japan) equipped with probe and image aberration correction operated at 200 kV. All STEM images were Fourier-filtered using a lattice mask to remove noise. The accurate positions of the *A*/*B*-site atomic columns were determined by fitting a two-dimensional Gaussian function, the angle and magnitude of polar displacements were calculated using a MATLAB script. The low electric field bipolar *P-E* loops at room temperature and frequency of 1 Hz were recorded by a ferroelectric tester (TF Analyzer 1000, aix ACCT, Germany) on bulk ceramics with a thickness of 0.5 mm and diameter of 10 mm. The dielectric temperature spectrum was tested by a dielectric spectrum measurement system (LDM-500, BALAB, China). The electrochemical impedance was measured with a precision impedance analyzer (4294A, Agilent, USA). The discharge characteristics, with an overdamped value of 13,000 Ω, were measured using Tongguo (TG) technology (CFD-003, Tongguo technology, China). The energy-storage properties were determined by measuring the unipolar *P-E* loops of the fatigued samples under 40 $kV \cdot mm^{-1}$ at 10 Hz (Radiant Technologies, USA). The neutron total scattering experiments were conducted at room temperature on the Spallation Neutron Source (SNS, Oak Ridge National Laboratory). The UV-Vis diffuse reflectance spectra (DRS) were recorded by a Persee T9S spectrophotometer (China), $BaSO_4$ was used a reflectance standard.

The Bragg Rietveld refinement was done with GSAS-II software, using the neutron data from four banks (bank 2~5) to get the long-range average structure parameters. Reverse Monte Carlo (RMC) simulation was performed based on the RMCprofile software[35,36]. The 20×20×20 supercells of pseudocubic (*Pm*-3*m*) structure (about 80×80×80 $Å^3$) containing 40,000 atoms and randomly distributed *A*-site atoms were established. In the RMC simulations, the Bragg intensities, *G*(*r*) and *S*(*Q*) data were fitted simultaneously under the bond valence sum and coordination constraints. *A*-site atoms were allowed to swap, and each RMC modelling was run to generate more than 10^3 move per atom to get converged. Detailed analysis of 3D polar displacements, unit-cell polar vectors, and polar projection can be referred to our previous works[21,22]. To get the statistical analysis results, 20 refined 3D atom configurations were merged together.

From the refined atom configurations, for each *A* site atoms ($\vec{r}_A$), the coordinates of the neighboring oxygen atoms ($\vec{r}_{O_i}$) can be extracted. The geometric center of the AO_{12} polyhedra can be calculated as $\frac{1}{12}\sum_i \vec{r}_{O_i}$. Similarly, the surrounding six oxygen atoms $\vec{r}_{O_i}$ of each *B* site atom ($\vec{r}_B$) can be found. The *A* site atom polar displacement vector $\vec{D}_A$ and the *B* site atom polar displacement vector $\vec{D}_B$ can be calculated by the Equation (1) and Equation (2), respectively[37]. Notably, the *A*-site atom without 12 physically reasonable oxygen bonds, or these *B*-site atom without 6 physically reasonable oxygen bonds were discarded.

$$\vec{D}_A = \vec{r}_A - \frac{1}{12}\sum_i \vec{r}_{O_i} \quad (1)$$

$$\vec{D}_B = \vec{r}_B - \frac{1}{6}\sum_i \vec{r}_{O_i} \quad (2)$$

For unit-cell polar vector calculation, one perovskite unit cell contains 8 *A* site atoms, 1 *B* site atom, and 6 O atoms. Firstly, the coordinates of 6 neighboring oxygen atoms ($\vec{r}_{O_i}$), and the coordinates of 8 neighboring *A* site atoms $\vec{r}_{A_i}$ of each *B* site atom $\vec{r}_{B_i}$ can be found. In the perovskite unit-cell, the center of the oxygen polyhedral is $\frac{1}{6}\sum_i \vec{r}_{O_i}$, and the center of the *A* site atom is $\frac{1}{8}\sum_i \vec{r}_{A_i}$. Subsequently, the unit-cell polar vector ($\vec{P}$) can be calculated by Equation 3[37]:

$$\vec{P} = \frac{q_A \times (\frac{1}{8}\sum_i \vec{r}_{A_i} - \frac{1}{6}\sum_i \vec{r}_{O_i}) + q_B \times (\vec{r}_{B_i} - \frac{1}{6}\sum_i \vec{r}_{O_i})}{V} \quad (3)$$

Where the *q* indicates the ion charge, *V* is the perovskite unit-cell volume.

RESULTS AND DISCUSSION

The BNT-BT-*x*BS (x = 0, 0.06, 0.10, 0.12) Pb-free ceramic system was synthesized via a solid-state reaction method. For x = 0, a characteristic ferroelectric *P*-*E* loop with a high P_m of 24.1 μC·cm^{-2} and a large P_r of 20.2 μC·cm^{-2} is observed, confirming robust long-range ferroelectric ordering. With increasing concentration of BS, the *P*-*E* loops gradually evolve into slim-shaped ones with greatly reduced P_r, thereby resulting in an ultrahigh η of 90% when x = 0.1 [Supplementary Figure 1]. The dielectric relaxation behavior is also enhanced with increasing x, as evidenced by the increased frequency dispersion in the ε_r-*T* spectra, further confirming the strengthening of relaxor characteristics [Supplementary Figure 2]. The XRD patterns of BNT-BT-*x*BS ceramics are shown in Supplementary Figure 1B. All compositions exhibit a single-phase perovskite structure without detectable impurity phases. With increasing BS content, the ceramic sample gradually transits from a tetragonal (*T*) phase toward a pseudo-cubic phase. Concurrently, the diffraction peaks shift to lower angles, indicating the lattice expansion driven by the substitution of larger Ba^{2+} and Sn^{4+} ions for the *A*-/*B*-sites of BNT-BT lattice respectively [Supplementary Figure 1C].

Figure 2A displays the high-resolution transmission electron microscope (TEM) of BNT-BT-0.1BS ceramics, which shows a long-range average cubic structure [Figure 2B and C, Supplementary Figure 1C]. Moreover, the Inverse fast Fourier transform (IFFT) shows obvious local lattice distortions, revealing the existence of polar nanoregions (PNRs), rather than macroscopic ferroelectric domains. To further resolve the polar structural characteristics of the x = 0.10, atomic-resolution imaging along the $[100]_c$ was performed via HAADF-STEM. The positions and relative intensities of *A*/*B*-site atoms were precisely determined using two-dimensional Gaussian function fitting, and atomic displacement vectors were calculated by quantifying the deviation of *B*-site atoms from the center of their four nearest-neighbor *A*-site atoms. The atomic displacement vector maps illustrate both the magnitude (arrow's length) and directional correlation (arrow's color) of local displacements. Obviously, the polar clusters with size of approximately 2-5 nm are observed [Figure 2D]. These clusters corresponding to *T*, rhombohedral (*R*), and/or orthogonal (*O*) structures are interconnected via weaker displacements with low symmetries [Figure 2E-G], confirming the coexistence of local structural distortions within the long-range cubic framework. This observation is further supported by the diverse *c*/*a* ratios [Figure 2H]. Despite the average pseudo-cubic symmetry of the x = 0.10, the local distortions reach up to 8% [Figure 2H], highlighting the beneficial role of lattice expansion and structural mismatch in enhancing the local polarization. The intensity of atomic columns in HAADF images is proportional to the atomic number (*Z*)[38]. As shown in Figure 2I, distinct intensity variations reflect local compositional fluctuations, where weaker-intensity regions correspond to Na-rich domains (Z_{Na} = 11), and stronger-intensity regions arise from Bi-rich domains (Z_{Bi} = 83). This atomic chemical inhomogeneity is the

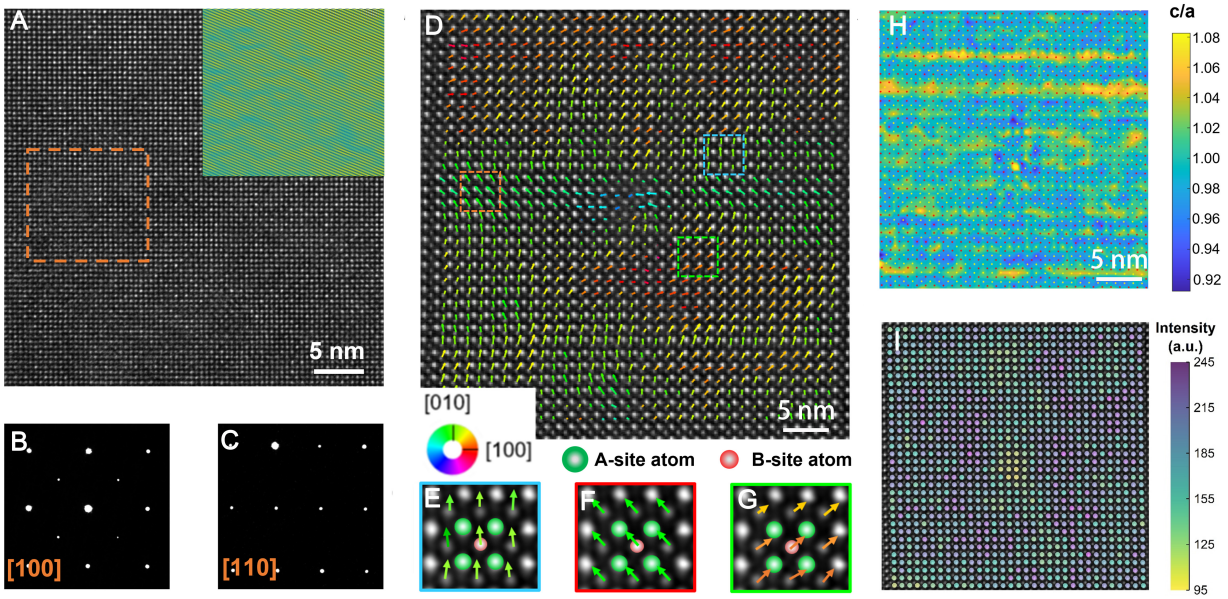

Figure 2. Microscopic structure of BNT-BT-0.1BS ceramic observed by electron microscopy. (A) High-resolution TEM image and corresponding IFFT pattern in the inset; (B and C) SAED patterns along the $[001]_c$ and $[110]_c$ directions; (D) HAADF-STEM image recorded along the $[100]_c$ direction and the corresponding atomic displacement vector mapping; (E-G) Enlarged *B*-site displacement vectors of the boxed region in (D). Corresponding (H) *c*/*a* ratio, and (I) atomic intensity mapping of (D). BNT: $Bi_{0.5}Na_{0.5}TiO_3$; BT: $BaTiO_3$; BS: $BaSnO_3$; TEM: transmission electron microscope; IFFT: inverse fast Fourier transform; SAED: selected area electron diffraction; HAADF-STEM: high-angle annular dark-field scanning transmission electron microscopy.

main reason for the local polarization fluctuations and structural distortions, which are beneficial for the increment in P_m and decrement in hysteresis loss, thereby advancing the energy-storage performance.

The atomic displacement derived from the HAADF-STEM in Figure 2 reveals only a two-dimensional distribution, lacking the access to ion-specific polarity information. However, the atomic pair distribution function (PDF) based on the neutron total scattering can reveal the influence of chemical composition on local structural evolution and the role of foreign ions in constructing polar structures[39,40]. Furthermore, a three-dimensional atomic model can be established using the Reverse Monte Carlo (RMC) algorithm, achieving enhanced structural precision through joint refinement of neutron real-space PDF $G(r)$, reciprocal-space scattering function $S(Q)$, and Bragg diffraction data [Figures 3A-C][35,41,42]. The polyhedral network in perovskite oxides provides a reference framework for calculating the local and nanoscale structures [Figure 3D]. Figure 3E and F illustrate the stereographic projections of atomic polar displacements along the $[001]_c$. Bi^{3+} ions exhibit strong preferential polar displacements along the *T*-direction accompanied by relatively weaker *R*-directional preferences. This similar polarization behavior is also reported in other Bi-based compounds[19-21]. In contrast, Ti^{4+} displacement vectors display pronounced directional disorder.

To further disclose the symmetry/asymmetry distribution of oxygen atoms around distinct elements, element-specific *A*/*B*-O PDFs are extracted and presented in Figure 3G. The pronounced splitting of the Bi-O pair originates from the strong hybridization between Bi $6s^2$ lone-pair electrons and O 2*p* orbitals, while the asymmetric peak of the Na-O pair is attributed to the steric hindrance effect induced by the small ionic radius of Na^+. Moreover, the Sn-O pair does not exhibit noticeable splitting but shifts relative to the Ti-O peak, indicating that Sn^{4+} incorporation disrupts long-range coherence of local polar displacements, driving an order-to-disorder transition without significantly reducing displacement magnitudes. This evolution manifests macroscopically as enhanced relaxor ferroelectric behavior and a diffuse dielectric response. Calculated average polarization displacement parameters (*D*) for *A*/*B*-site ions are 0.18, 0.39, 0.34, 0.19, and

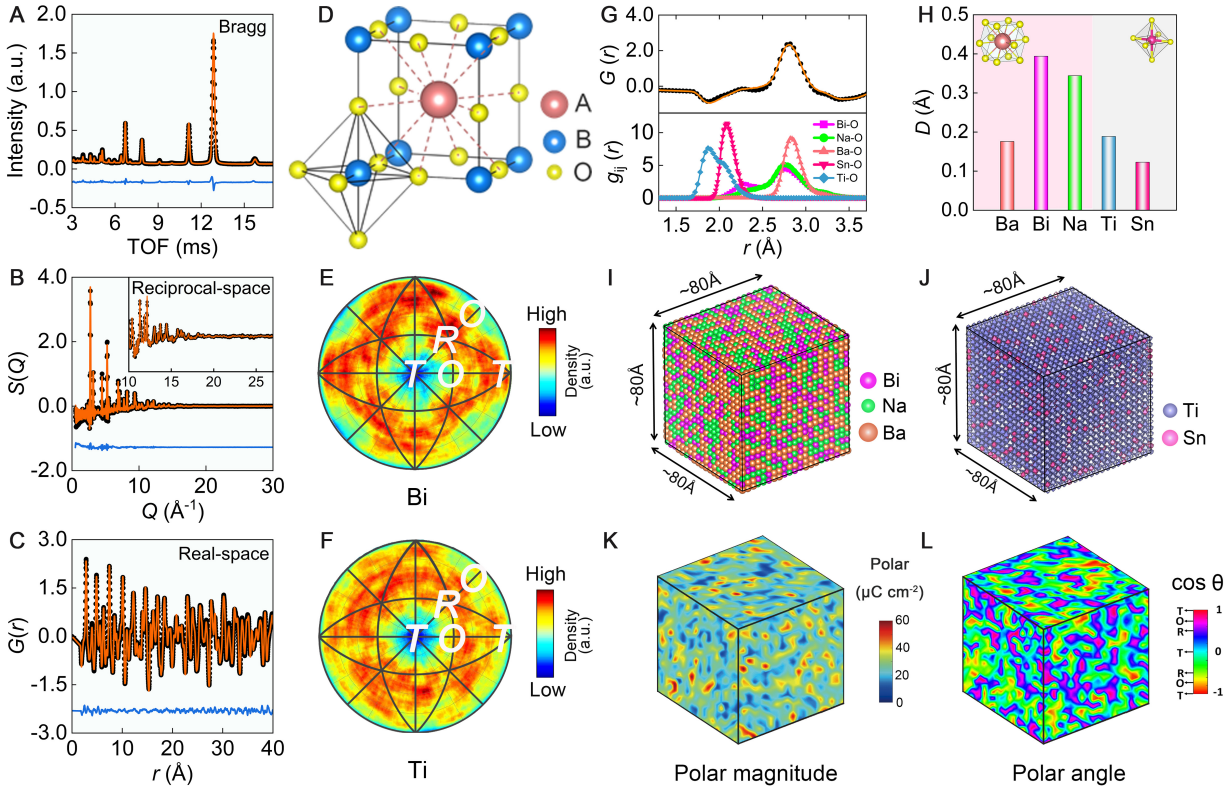

Figure 3. Local structures of BNT-BT-0.1BS refined by RMC fitting and neutron total scattering. (A-C) Fitting results of neutron scattering data, including Bragg data, *S*(*Q*) and *G*(*r*); (D) Perovskite ABO_3 structure with a polyhedral network; (E and F) Stereographic projections of atomic polar displacement vectors along the $[001]_c$ direction; (G) Experimental and calculated pair distribution functions *G*(r) and correlation analysis of nearest-neighbor atomic pairs within the range of 1.3-3.7 Å; (H) Average amplitude of polar displacements; (I and J) Three-dimensional distribution images of *A*-site and *B*-site atoms, respectively; (K and L) Three-dimensional polar amplitude and polar angle distributions, respectively. BNT: $Bi_{0.5}Na_{0.5}TiO_3$; BT: $BaTiO_3$; BS: $BaSnO_3$; RMC: reverse Monte Carlo; TOF: time of flight.

0.12 Å for Ba^{2+}, Bi^{3+}, Na^{+}, Ti^{4+}, and Sn^{4+}, respectively [Figure 3H]. Combined analysis of *A*/*B*-site chemical heterogeneity and unit-cell polarization vectors [Figure 3I-L], it is found that the incorporation of BS effectively disrupts the long-range ferroelectric domains and facilitates the formation of strong polar nanoclusters with coexistence of *T*, *R* and *O* symmetries [Figure 3L], consistent with atomic displacement in Figure 2D. Notably, the high polarization displacement of Bi^{3+} in the ferroelectric matrix is largely retained in the relaxor state. Accordingly, in regions enriched with Bi^{3+}, the unit-cell polarization magnitude reaches as high as ~60 μC·cm^{-2} [Figure 3K], demonstrating significant local polar fluctuations. These results confirm the feasibility of local structure design and chemical modulation through the coupling of ferroelectric units with high structural distortion and polar units with lattice expansion. This strategy is crucial for achieving high polarization, slim hysteresis behavior, and exceptional energy storage performance.

Based on the local structure and rational chemical design, BNT-BT-0.1BS ceramic presents remarkable energy-storage performance. As illustrated in Figure 4A, BNT-BT-0.1BS ceramic consistently exhibits slim *P*-*E* loops with low P_r and high P_m over a wide electric field range of 10-70 kV·mm^{-1}. Notably, benefiting from the electro-polarization effect, a high P_m of 35.5 μC·cm^{-2} is achieved at 20 kV·mm^{-1}. As the applied field increases from 20 kV·mm^{-1} to the breakdown field (E_B = 70 kV·mm^{-1}), P_m rises significantly from 35.5 to 60 μC·cm^{-2}, which can be attributed to the characteristic local structure. However, even at such a high electric field, polarization saturation is not observed, indicating an enhanced high-field polarization capability. Additionally, the P_r retains as low as 7 μC·cm^{-2}, leading to a large ΔP of 53 μC·cm^{-2}, which is conducive to realize an ultrahigh W_{rec}.

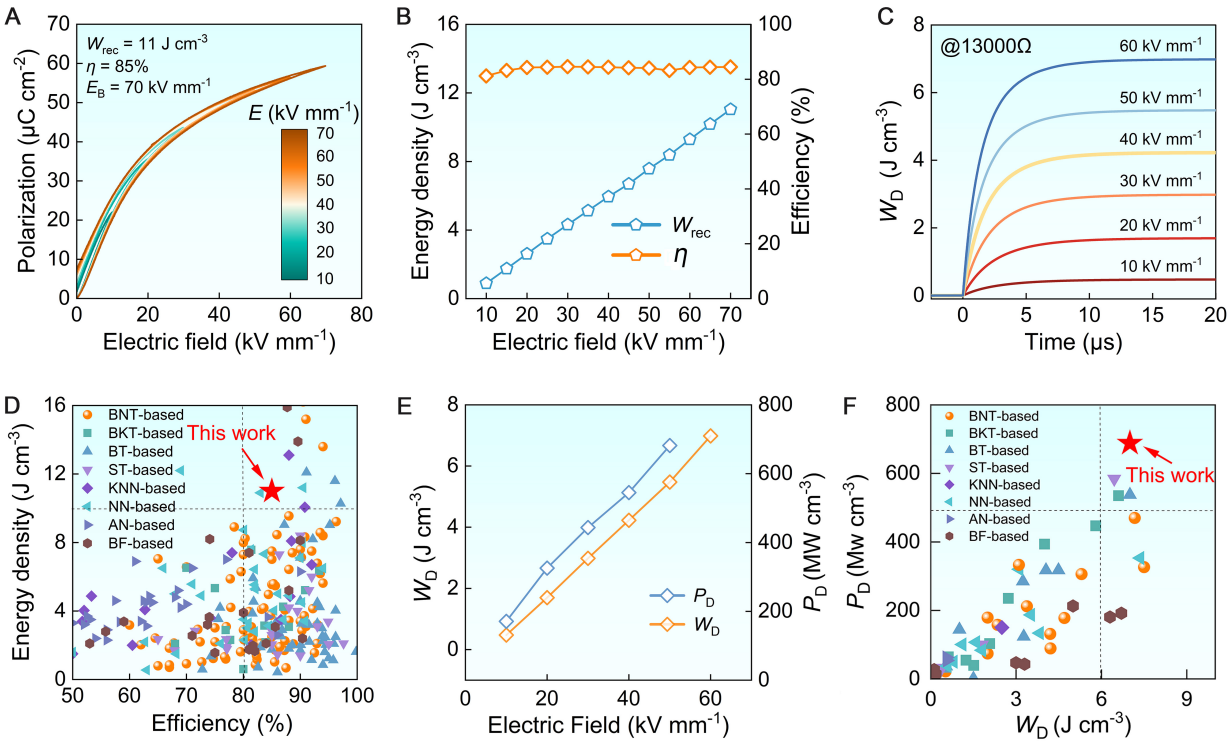

Figure 4. Energy-storage performance of BNT-BT-0.1BS ceramics. (A) Unipolar *P-E* loops under different electric fields, and (B) corresponding W_{rec} and η; (C) Variation of W_D with time under different electric fields; (D) Comparison of W_{rec} and η with reported Pb-free bulk ceramics; (E) Comparison of P_D and W_D with reported Pb-free bulk ceramics; (F) W_D and P_D under different electric fields. BNT: $Bi_{0.5}Na_{0.5}TiO_3$; BT: $BaTiO_3$; BS: $BaSnO_3$; BKT: $Bi_{0.5}K_{0.5}TiO_3$; ST: $SrTiO_3$; KNN: $K_{0.5}Na_{0.5}NbO_3$; NN: $NaNbO_3$; AN: $AgNbO_3$; BF: $BiFeO_3$.

Excitingly, BNT-BT-0.1BS ceramic sample exhibits an ultranarrow hysteresis loop, along with a high P_m of 60 μC·cm^{-2}, a high E_B of 70 kV·mm^{-1}, an impressive W_{rec} of 11 J·cm^{-3}, and a high η of 85%, delivering the desired "dual-high" energy-storage performance [Figure 4A and B]. Compared with other reported Pb-free bulk dielectric ceramics, BNT-BT-0.1BS exhibits superior energy-storage performance and charge-discharge capability [Figure 4C and D], validating the effectiveness of the polar structure and chemistry-guided design strategy. Moreover, the charge-discharge capability is another crucial parameter for evaluating the practical potential of energy-storage ceramics. The overdamped charge-discharge characteristics of BNT-BT-0.1BS are systematically evaluated under different electric fields [Figure 4C]. The W_D increases with electric field and reaches 7.0 J·cm^{-3} at 60 kV·mm^{-1}, accompanied by a fast discharge time of $t_{0.9}$ = 4.3 μs. Furthermore, a high-power density (P_D) of 688 MW·cm^{-3} is achieved at 50 kV·mm^{-1} [Figure 4E and Supplementary Figure 3]. As shown in Figure 4F, the P_D and W_D of BNT-BT-0.1BS ceramic far surpasses those of other reported bulk dielectric ceramics, highlighting its outstanding charge-discharge capability. Therefore, BNT-BT-0.1BS holds great promise as a Pb-free, eco-friendly, and high-performance candidate for advanced energy-storage capacitors.

Such superior energy-storage performance mainly originates from the synergistic contributions of multiple factors, including high P_m, low P_r, slim hysteresis, and high E_B. The high P_m is ascribed to the large structural distortion induced strong local polar clusters, and enhanced polarization flexibility stemming from Ba^{2+}-driven lattice expansion. The reduced P_r and slim hysteresis stem from the modification of the *B*-site chemical environment by Sn^{4+}, which introduces random fields by disturbing atomic order and suppressing long-range polarization correlations. The high E_B achieved in this study originates from the synergistic optimization of the material's microstructure and electrical properties. First, the ceramic samples exhibit a highly dense microstructure (relative density > 93%) and a uniformly distributed fine-grained structure

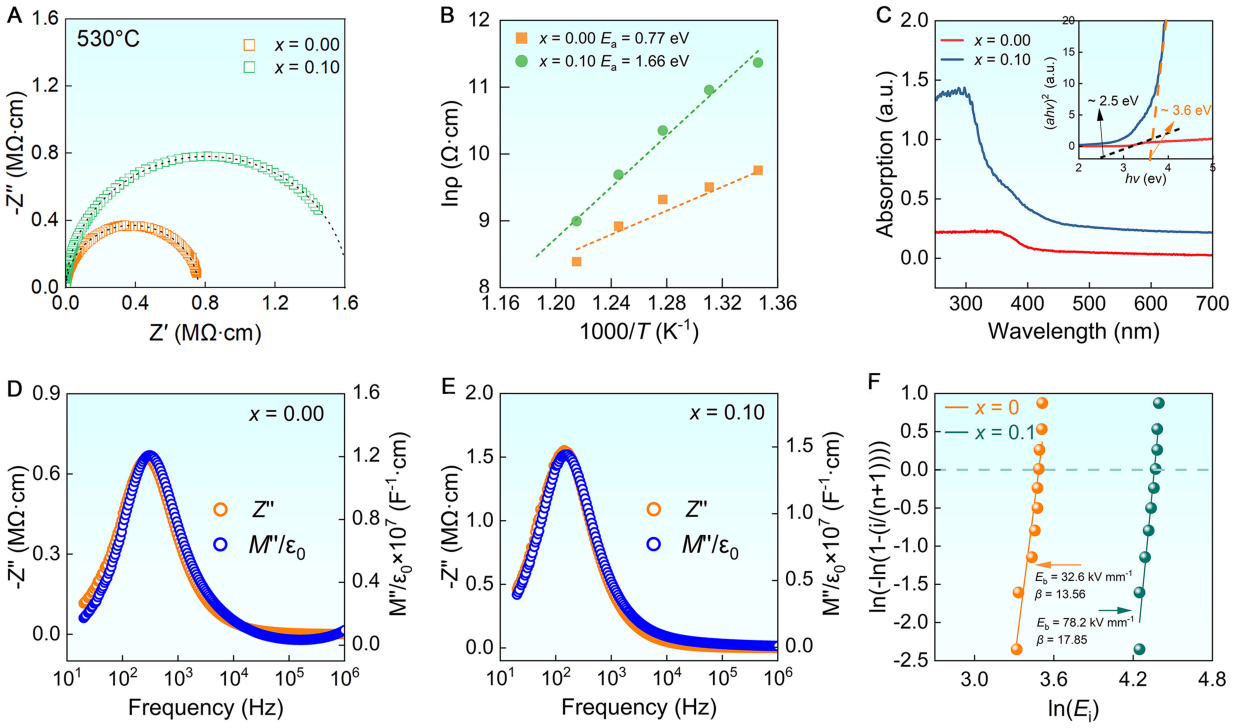

Figure 5. Electrical microstructures of BNT-BT-*x*BS ceramics. (A) Impedance profiles at 530 °C of x = 0, 0.10; (B) Activation energy (E_a) of x = 0, 0.10; (C) UV-Vis absorption spectrum of x = 0, 0.10 with calculated band gap (E_g); (D and E) Spectroscopic plots of Z'' and M'' spectra at 530 °C of x = 0 and 0.10; (F) Weibull distribution of the E_B for x = 0, 0.10. BNT: $Bi_{0.5}Na_{0.5}TiO_3$; BT: $BaTiO_3$; BS: $BaSnO_3$; UV-Vis: ultraviolet-visible.

(~1 μm) [Supplementary Figures 4 and 5]. These structural characteristics effectively reduce defects such as pores that concentrate electric fields, while the high-density grain boundary network hinders the propagation of conductive pathways, thereby enhancing breakdown toughness. Simultaneously, the introduction of the BS component significantly improves the electrical performance of the material: impedance spectroscopy analysis indicates that the x = 0.10 sample exhibits the highest resistivity [Figure 5A, Supplementary Figure 6] and a relatively high activation energy (E_a = 1.66 eV, Figure 5B), suggesting lower carrier mobility compared to the base composition (x = 0)[43]. UV-Vis spectroscopy reveals that the bandgap of this composition expands to approximately 3.6 eV [Figure 5C], raising the intrinsic breakdown threshold. Notably, the nearly coincident frequencies of the Z″ and M″ peaks in the impedance and modulus spectra reflect a near-ideal Debye relaxation behavior, indicating good electrical homogeneity of the material [Figure 5D and E][44]. These comprehensive factors yield a lower possibility of a breakdown, thereby resulting in a narrow distribution of the highest applied E and a large E_B of 78.2 kV·mm^{-1} [Figure 5F].

The stability in energy-storage performance is also crucial for the usage of dielectric capacitors in the harsh environment. Interestingly, BNT-BT-0.1BS ceramic exhibits excellent frequency reliability, temperature stability, and fatigue resistance under 40 kV·mm^{-1} [Figure 6]. Evidently, all the obtained P-E loops are narrow, with a stable W_{rec} ~ 6.44 ± 0.17 J·cm^{-3} and a low variation of η within 1.4% under various frequencies from 1 to 200 Hz [Figure 6A and B]. When the accumulative cycling number reaches to 10^6, both W_{rec} and η show a slight variation within 1%, suggesting excellent fatigue resistance [Figure 6C and D]. Simultaneously, the ceramic also presents high thermal stability from RT to 140 °C, with W_{rec} ~ 6.55 ± 0.12 J·cm^{-3} and η variation < 2.1% [Figure 6E and F]. All these show the application potential of BNT-BT-0.1BS in the field of energy-storage capacitors.

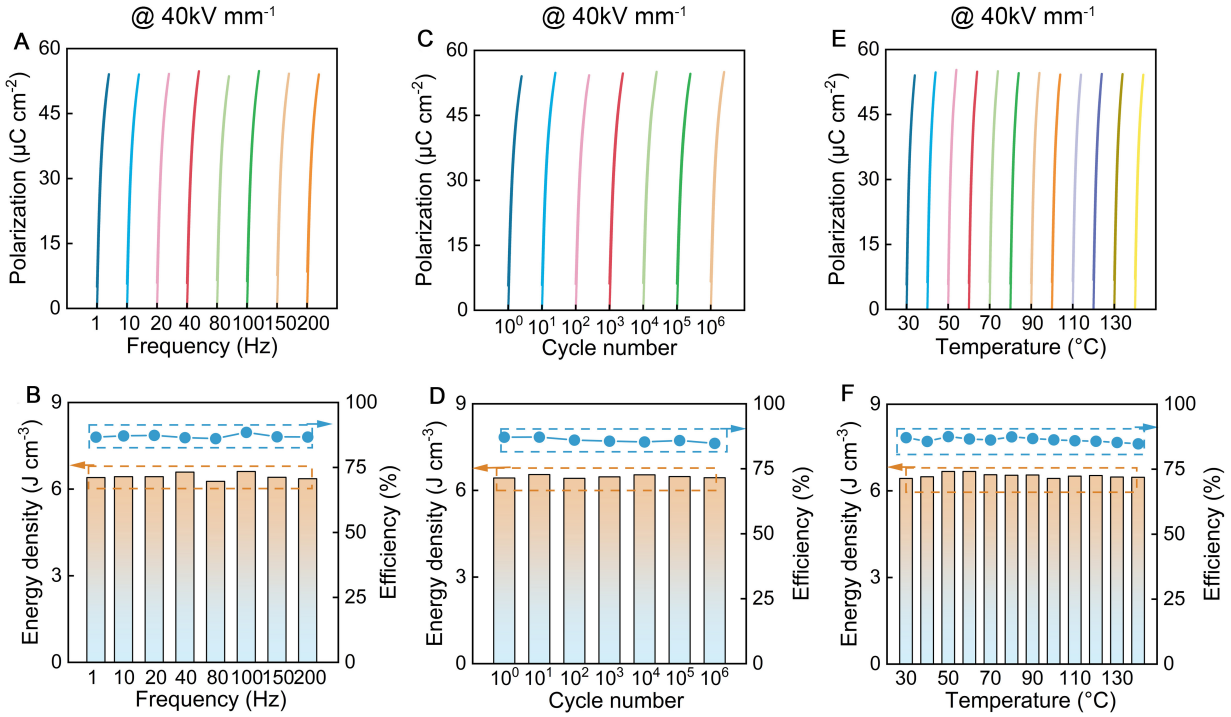

Figure 6. Stability in energy-storage performance for BNT-BT-0.1BS ceramics. (A and B) frequency-, (C and D) cycling number- and (E and F) temperature-dependent unipolar *P-E* curves and corresponding W_{rec} and η at 40 kV·mm^{-1}. BNT: $Bi_{0.5}Na_{0.5}TiO_3$; BT: $BaTiO_3$; BS: $BaSnO_3$.

CONCLUSIONS

This work demonstrates a rational design strategy for high-performance Pb-free RFEs by coupling lattice-expanding Ba^{2+} and order-disrupting Sn^{4+} in BNT-BT ceramics, providing a novel pathway for the rational design of high-performance lead-free energy-storage materials. The key innovations are: Firstly, a novel compositional design principle based on the synergistic regulation of t and δ was proposed and validated, enabling the coexistence of strong intrinsic polarization and enhanced relaxor characteristics. Secondly, the atomic-scale mechanism of synergy between "lattice expansion for enhanced polarization flexibility" and "*B*-site chemical frustration for breaking long-range order" was unraveled. Neutron total scattering and atomic-resolution STEM confirmed the formation of strong polar nanoclusters (2-5 nm) with intense local polarization up to ~60 μC·cm^{-2}, featuring a mixture of rhombohedral, tetragonal, and orthorhombic symmetries. Thirdly, a breakthrough in comprehensive energy-storage performance was achieved. The optimized ceramic exhibits not only a high recoverable energy density (11 J·cm^{-3}) and high efficiency (85%), but also superior discharge capability (power density of 688 MW·cm^{-3}), high breakdown strength (~70 kV·mm^{-1}), and excellent stability over frequency, temperature, and cycling. This strategy holds promise for extension to other ferroelectric systems and offers a material foundation for developing practical energy-storage devices with high energy density, high efficiency, and high power output.

DECLARATIONS

Authors' contributions

Experiment, characterization: Zhu, Z.; Zha, Y.; Wang, S.; Luo, Z.
Investigation, methodology: Zhu, Z.; Luo, H.
Wring origin draft: Zhu, Z.; Zhang, J.; Luo, H.
Writing-review and editing: Zhu, L. F.; Liu, H.
Supervision: Liu, L.; Zhang, G.
Funding acquisition: Zhang, J.; Liu, H.

Availability of data and materials

Data supporting the findings of this study are available from the corresponding author upon reasonable request.

AI and AI-assisted tools statement

Not applicable.

Financial support and sponsorship

This work was supported by the National Natural Science Foundation of China (Nos. 22471013 and 12374085).

Conflicts of interest

All authors declared that there are no conflicts of interest.

Ethical approval and consent to participate

Not applicable.

Consent for publication

Not applicable.

Supplementary Materials

Supplementary Materials

REFERENCES

1. Cheema, S. S.; Shanker, N.; Hsu, S.; et al. Giant energy storage and power density negative capacitance superlattices. *Nature* **2024**, *629*, 803-9. DOI PubMed
2. Zhang, M.; Lan, S.; Yang, B. B.; et al. Ultrahigh energy storage in high-entropy ceramic capacitors with polymorphic relaxor phase. *Science* **2024**, *384*, 185-9. DOI PubMed
3. Yang, L.; Kong, X.; Li, F.; et al. Perovskite lead-free dielectrics for energy storage applications. *Prog. Mater. Sci.* **2019**, *102*, 72-108. DOI
4. Li, J.; Shen, Z.; Chen, X.; et al. Grain-orientation-engineered multilayer ceramic capacitors for energy storage applications. *Nat. Mater.* **2020**, *19*, 999-1005. DOI PubMed
5. Li, Q.; Chen, L.; Gadinski, M. R.; et al. Flexible high-temperature dielectric materials from polymer nanocomposites. *Nature* **2015**, *523*, 576-9. DOI PubMed
6. Yang, B.; Zhang, Y.; Pan, H.; et al. High-entropy enhanced capacitive energy storage. *Nat. Mater.* **2022**, *21*, 1074-80. DOI PubMed
7. Wang, G.; Lu, Z.; Li, Y.; et al. Electroceramics for high-energy density capacitors: current status and future perspectives. *Chem. Rev.* **2021**, *121*, 6124-72. DOI PubMed PMC
8. Jang, J.; Choi, S. Reduced dimensional ferroelectric domains and their characterization techniques. *Microstructures* **2024**, *4*, 2024016. DOI
9. Yan, F.; Qian, J.; Lin, J.; Ge, G.; Shi, C.; Zhai, J. Ultrahigh energy storage density and efficiency of lead-free dielectrics with sandwich structure. *Small* **2023**, *20*, 2306803. DOI PubMed
10. Jayakrishnan, A.; Silva, J.; Kamakshi, K.; et al. Are lead-free relaxor ferroelectric materials the most promising candidates for energy storage capacitors? *Prog. Mater. Sci.* **2023**, *132*, 101046. DOI
11. Kim, J.; Saremi, S.; Acharya, M.; et al. Ultrahigh capacitive energy density in ion-bombarded relaxor ferroelectric films. *Science* **2020**, *369*, 81-4. DOI PubMed
12. Liu, Y.; Zhang, Y.; Wang, J.; et al. Ultrahigh capacitive energy storage through dendritic nanopolar design. *Science* **2025**, *388*, 211-6. DOI PubMed
13. Zha, J.; Liu, J.; Yang, Y.; et al. High energy storage performance of (1-*x*)$Ba_{0.5}Sr_{0.5}TiO_3$-*x*$K_{0.5}Na_{0.5}NbO_3$ ceramics via a combined strategy of fine grains and multiphase polar nanoregions. *Chem. Eng. J.* **2024**, *486*, 150441. DOI
14. Zhao, L.; Liu, Q.; Gao, J.; Zhang, S.; Li, J. F. Lead-free antiferroelectric silver niobate tantalate with high energy storage performance. *Adv. Mater.* **2017**, *29*, 1701824. DOI PubMed

15. Ji, H.; Wang, D.; Bao, W.; et al. Ultrahigh energy density in short-range tilted NBT-based lead-free multilayer ceramic capacitors by nanodomain percolation. *Energy. Storage. Mater.* **2021**, *38*, 113-20. DOI
16. Yao, F.; Yuan, Q.; Wang, Q.; Wang, H. Multiscale structural engineering of dielectric ceramics for energy storage applications: from bulk to thin films. *Nanoscale* **2020**, *12*, 17165-84. DOI PubMed
17. Xi, K.; Liu, J.; Song, B.; et al. Boosting energy storage performance in negative temperature coefficient linear-like dielectrics via composite modulation in the superparaelectric state. *J. Eur. Ceram. Soc.* **2024**, *44*, 1588-96. DOI
18. Zhang, M.; Zhu, M.; Chang, Z.; et al. Achieving excellent energy storage performance of $K_{1/2}Bi_{1/2}TiO_3$-based ceramics via multi-phase boundary and bandgap engineering. *Chem. Eng. J.* **2023**, *473*, 145314. DOI
19. Pan, H.; Lan, S.; Xu, S.; et al. Ultrahigh energy storage in superparaelectric relaxor ferroelectrics. *Science* **2021**, *374*, 100-4. DOI PubMed
20. Liu, Z.; Peng, H.; Lu, T.; et al. Harnessing multisite high-entropy architecture for ultrahigh energy storage multilayer capacitors. *J. Am. Chem. Soc.* **2025**, *147*, 41620-8. DOI PubMed
21. Liu, H.; Sun, Z.; Zhang, J.; et al. Chemical design of Pb-free relaxors for giant capacitive energy storage. *J. Am. Chem. Soc.* **2023**, jacs.3c02811. DOI PubMed
22. Chen, Y.; Zhu, Z.; Zhu, L.; et al. Giant capacitive energy-storage in $BaTiO_3$-based fine-grained relaxors via local polarization enhancement. *Adv. Mater.* **2025**, *37*, 2420566. DOI PubMed
23. Qi, H.; Xie, A.; Tian, A.; Zuo, R. Superior energy-storage capacitors with simultaneously giant energy density and efficiency using nanodomain engineered $BiFeO_3$-$BaTiO_3$-$NaNbO_3$ lead-free bulk ferroelectrics. *Adv. Energy. Mater.* **2019**, *10*, 1903338. DOI
24. Pan, H.; Li, F.; Liu, Y.; et al. Ultrahigh-energy density lead-free dielectric films via polymorphic nanodomain design. *Science* **2019**, *365*, 578-82. DOI PubMed
25. Wang, X.; Song, X.; Fan, Y.; et al. Lead-free high permittivity quasi-linear dielectrics for giant energy storage multilayer ceramic capacitors with broad temperature stability. *Adv. Energy. Mater.* **2024**, *14*, 2400821. DOI
26. Qi, H.; Chen, L.; Deng, S.; Chen, J. High-entropy ferroelectric materials. *Nat. Rev. Mater.* **2023**, *8*, 355-6. DOI
27. Long, C.; Zhou, W.; Song, H.; et al. Simultaneously realizing ultrahigh energy storage density and efficiency in $BaTiO_3$-based dielectric ceramics by creating highly dynamic polar nanoregions and intrinsic conduction. *Acta. Mater.* **2023**, *256*, 119135. DOI
28. Yang, F.; Bao, Y.; Zeng, B.; et al. Excellent energy storage properties in ZrO_2 toughened $Ba_{0.55}Sr_{0.45}TiO_3$-based relaxor ferroelectric ceramics via multi-scale synergic regulation. *Chem. Eng. J.* **2024**, *493*, 152624. DOI
29. Li, D.; Meng, X.; Zhou, E.; et al. Ultrahigh energy density of antiferroelectric $PbZrO_3$-based films at low electric field. *Adv. Funct. Mater.* **2023**, *33*, 2302995. DOI
30. Pan, H.; Ma, J.; Ma, J.; et al. Giant energy density and high efficiency achieved in bismuth ferrite-based film capacitors via domain engineering. *Nat. Commun.* **2018**, *9*, 1813. DOI PubMed PMC
31. Cao, W.; Lin, R.; Hou, X.; et al. Interfacial polarization restriction for ultrahigh energy-storage density in lead-free ceramics. *Adv. Funct. Mater.* **2023**, *33*, 2301027. DOI
32. Ding, Y.; Li, P.; He, J.; et al. Simultaneously achieving high energy-storage efficiency and density in Bi-modified SrTiO3-based relaxor ferroelectrics by ion selective engineering. *Compos. Part. B. Eng.* **2022**, *230*, 109493. DOI
33. Corker, D. L.; Glazer, A. M.; Whatmore, R. W.; Stallard, A.; Fauth, F. A neutron diffraction investigation into the rhombohedral phases of the perovskite series. *J. Phys. Condens. Matter.* **1998**, *10*, 6251-69. DOI
34. Wang, K.; Li, J. Analysis of crystallographic evolution in (Na,K)NbO3-based lead-free piezoceramics by x-ray diffraction. *Appl. Phys. Lett.* **2007**, *91*, 262902. DOI
35. Tucker, M. G.; Keen, D. A.; Dove, M. T.; Goodwin, A. L.; Hui, Q. RMCProfile: reverse Monte Carlo for polycrystalline materials. *J. Phys. Condens. Matter.* **2007**, *19*, 335218. DOI PubMed
36. Krayzman, V.; Levin, I.; Woicik, J. C.; Bridges, F. Correlated rattling-ion origins of dielectric properties in reentrant dipole glasses $BaTiO_3$-$BiScO_3$. *Appl. Phys. Lett.* **2015**, *107*, 192903. DOI
37. Datta, K.; Margaritescu, I.; Keen, D.; Mihailova, B. Stochastic polarization instability in $PbTiO_3$. *Phys. Rev. Lett.* **2018**, *121*, 137602. DOI PubMed
38. Pennycook, S. J.; Boatner, L. A. Chemically sensitive structure-imaging with a scanning transmission electron microscope. *Nature* **1988**, *336*, 565-7. DOI
39. Petkov, V. Nanostructure by high-energy X-ray diffraction. *Mater. Today.* **2008**, *11*, 28-38. DOI
40. Keen, D. A. Total scattering and the pair distribution function in crystallography. *Crystallogr. Rev.* **2020**, *26*, 143-201. DOI
41. Zhang, Y.; Eremenko, M.; Krayzman, V.; Tucker, M. G.; Levin, I. New capabilities for enhancement of *RMCProfile*: instrumental profiles with arbitrary peak shapes for structural refinements using the reverse Monte Carlo method. *J. Appl. Crystallogr.* **2020**, *53*, 1509-18. DOI

42. Wang, L.; Qi, H.; Deng, S.; et al. Design of superior electrostriction in $BaTiO_3$-based lead-free relaxors via the formation of polarization nanoclusters. *InfoMat* **2022**, *5*, e12362. DOI

43. Ogihara, H.; Randall, C. A.; Trolier-mckinstry, S. High-energy density capacitors utilizing 0.7 $BaTiO_3$-0.3 $BiScO_3$ ceramics. *J. Am. Ceram. Soc.* **2009**, *92*, 1719-24. DOI

44. Chen, F.; Chen, M.; Zhang, J.; et al. Polar vortices in relaxor ferroelectric ceramics for high-efficiency capacitive energy storage. *ACS. Nano.* **2025**, *19*, 1809-18. DOI PubMed